PAPER

Check for updates

An air-stable ultraviolet photodetector based on mesoporous TiO$_2$/spiro-OMeTAD

Huiwen Bai, Ting Shen and Jianjun Tian [ID] *

A hybrid organic/inorganic heterojunction structured photodetector has attracted much attention due to its high device stability and ease of fabrication. In this work, an ultraviolet photodetector with the configuration of spiro-OMeTAD/mesoporous TiO$_2$/compact TiO$_2$ was developed. The small molecule of spiro-OMeTAD was introduced as the active layer, owing to its fast response to the ultraviolet light and high glass transition temperature (T_g). The mesoporous TiO$_2$ layer with a large specific area could accelerate the interface separation of electrons and holes, while the compact TiO$_2$ layer was used to block the charge leakage between FTO and spiro-OMeTAD. With a 100 nm TiO$_2$ mesoporous layer, the photodetector displayed a fast response time (<0.02 s), a low dark current density (8.79 nA cm^{-2}) and a high detectivity (3.5 × 10^{13} Jones) at 340 nm light wavelength and a 0.60 V voltage output. Besides, the unencapsulated device in air also showed excellent long-term stability (~2 months) and thermal stability (~100 °C).

1 Introduction

Owing to the light weight, low index of refraction and mechanical flexibility, organic semiconductors such as fullerene, rubrene and pentacene have attracted attention as photodetectors in recent years.[1–4] These devices could be deposited onto a variety of substrates and produced at room temperature through several low-cost techniques, including solution processing and spin-coating.[5,6] Besides, the absorption coefficient and the range of organic molecules could also be controlled by co-evaporation or mixing of organic molecules. Thus, organic semiconductors show great potential as photodetectors.[7]

Generally, organic semiconductors were consisted of two categories of materials: small molecules and polymers.[8] In thin-layer devices, small molecules show higher speed communication in comparison with polymers.[9] Due to the good mutual solubility, it is also feasible to fabricate multilayer and complex structures with small molecules. Therefore, the small molecule materials have been widely used in thin-layer photoelectric devices, such as solar cells, organic light-emitting diodes (LEDs) and photodetectors.[10,11] However, the thermal stability of the mainly used molecules is still far from expectation.[12,13] For instance, triphenyldiamine (TPD) demonstrated a high hole mobility (3 × 10^{-3} cm^2 V^{-1} s^{-1}) at room temperature, but it will be amorphized when temperature is greater than its glass transition temperature (T_g = 65 °C).[14,15]

Fortunately, the spirocenter molecules could provide both superb charge transport properties and thermal stability, since

their T_g is up to 130 °C.[16–19] It is promising to achieve high durability, especially at high temperature. With this material, the device would exhibit peculiar architectural and electronic properties, which further enhanced the glass-forming capacity. When spirocenter molecules were combined with wide band-gap inorganic semiconductors, such as TiO$_2$ and ZnO, a hybrid organic/inorganic heterojunction could be formed. Xie *et al.* reported a self-powered photodetector based on TiO$_2$ nanorod/spiro-OMeTAD (2,2′,7,7″-tetrakis (*N,N*-di-*p*-methoxyphenyl-amine)-9,9′-spirobifluorene), which exhibited a high sensitivity under blue light.[20] After that, a photodetector with a ZnO nanorod/spiro-OMeTAD structure was also designed, which exhibited a fast response under ultraviolet and visible light.[21] In this hybrid organic/inorganic heterojunction structure, the nanostructured inorganic semiconductors provided a stable matrix and a large contacting surface area in the junction, while the filled organic semiconductor could significantly simplify the preparation procedure.[22,23]

Here, we reported a spiro-OMeTAD based ultraviolet light photodetector using compact layer and mesoporous film. Spiro-OMeTAD acted as a light harvesting material as well as a HTM. Mesoporous TiO$_2$ films composed of nanoparticles have a much larger surface area than that of previously reported nanorods. Such a large area could provide more paths for transportation of electrons, which is helpful for charge collection. In addition, the TiO$_2$ compact layer with a thickness of around 20 nm is usually used in the P–N junction photovoltaics, which can suppress the hole transfer into anodes so as to reduce the charge recombination. The thermal and air stabilities of the photodetector were completely characterized. The photodetector displayed a fast response time, a low dark current density, high

Institute of Advanced Materials and Technology, University of Science and Technology Beijing, 100083, China. E-mail: tianjianjun@mater.ustb.edu.cn

This journal is © The Royal Society of Chemistry 2017

J. Mater. Chem. C, 2017, **5**, 10543–10548 | **10543**

detectivity and a high output voltage. Most importantly, it exhibited excellent long-term and thermal stabilities and humidity resistance in air.

2 Experimental details

2.1 Materials

Titanium diisopropoxide bis (acetylacetonate) ($C_{16}H_{28}O_6Ti$, Sigma-Aldrich, 75%), TiO_2 (Degussa P25), ethanol (C_2H_5OH, Beijing China, ≥99.5%), 2,2′,7,7′-tetrakis (*N*,*N*-di-*p*-methoxyphenyl-amine)-9,9′-spirobifluorene (spiro-OMeTAD, 99.99%), 4-*tert*-butylpyridine ($C_9H_{13}N$, Sigma-Aldrich, 96%), bis(trifluoro-methane) sulfonimide lithium salt ($CF_3SO_2NLiSSO_2CF_3$, Sigma-Aldrich, 99.95%) were used. All chemicals were used directly without further purification.

2.2 Device fabrication

TiO_2 compact layers were coated on the clean FTO substrates using the thermal spraying technique, followed by annealing in air at 450 °C for 30 min. The compact TiO_2 precursor solution was prepared by diluting titanium diisopropoxide bis (acetyl-acetonate) (75 wt% in isopropanol) in ethanol in a volume ratio of 1 : 20. The thickness of the compact layer is around 20 nm. Afterwards, the TiO_2 nanoparticle (18 NRT, 1 : 12, 1 : 10 and 1 : 8 in wt with ethanol) dispersions were spin-coated on the as-prepared substrate with a speed of 5000 rpm and heated under conditions mentioned above. In this work, M-75, M-100 and M-140 represent the mesoporous structured photodetectors with a thickness of the mesoporous TiO_2 layers of 75 nm, 100 nm and 140 nm, respectively. The hole transfer layer was spin-coated by the chlorobenzene solution including 72.3 mg mL^{-1} spiro-OMeTAD, 28.8 μL mL^{-1} 4-*tert*-butylpyridine and 17.5 μL mL^{-1} bis(trifluoromethane) sulfonimide lithium salt (LiTFSI) solution at 4000 rpm for 30 s. The thickness of spiro-OMeTAD is about 220–260 nm and the thickness of all the samples remains the same. An Au counter electrode was fabricated by thermal evaporation. The active area was 1.007 cm^2.

For a planar structured photodetector, a TiO_2 compact layer was deposited on the FTO substrate as the electron transporting and hole blocking layer. As active and HTM layers, spiro-OMeTAD was spin-coated on the TiO_2 layer. Then, the Au layer was deposited on spiro-OMeTAD by thermal evaporation. For the mesoporous structured photodetectors, there is a TiO_2 mesoporous layer between the compact TiO_2 layer and the spiro-OMeTAD layer.

2.3 Characterization

The cross-sectional image of the mesoporous device was obtained using a high-resolution SEM (SU-8020, Hitachi). The absorption and transmission spectra were measured using an ultraviolet-visible (UV-Vis) spectrophotometer (UV-3600, Shimadzu). The photoluminescence (PL) spectra were recorded using a combined steady state & time resolved fluorescence spectro-meter (FLS980, Edinbergh). The UV light source was provided by a UV LED. The responsivity spectra were measured from an accessory of Zahner electrochemical workstation. The current

and voltage response spectra were also characterized from an accessory of Zahner electrochemical workstation with the assistance of a light source Zahner (PP211).

3 Results and discussion

Fig. 1a shows the planar and mesoporous configurations of the photodetectors. Fig. 1b exhibits the SEM cross-section image of the mesoporous structured device. Fig. 1c displays the energy diagram of the photodetector. Thus, the electrons and holes are excited at spiro-OMeTAD by photons to yield electron–hole pairs. The electrons are transferred through TiO_2 to FTO and the holes reach the Au electrode.

Fig. 2a shows the absorption spectra of the films of the mesoporous TiO_2 (MTO), spiro-OMeTAD and the heterojunction layer with MTO/spiro-OMeTAD. The spectrum of MTO shows little absorbance. However, spiro-OMeTAD shows the highest absorbance in the region of 350–400 nm, making it a potential candidate for fabricating a UV photodetector. The absorption peak of the MTO/spiro-OMeTAD film is slightly lower than that of spiro-OMeTAD. The possible reason is that the mesoporous layer makes FTO smoother and then reduces the light scatter, which results in the decrease of the absorption.[24] Fig. 2b displays the photoluminescence spectra of the films. The peak position is 430 nm with the same full width at half-maximum (FWHM) of
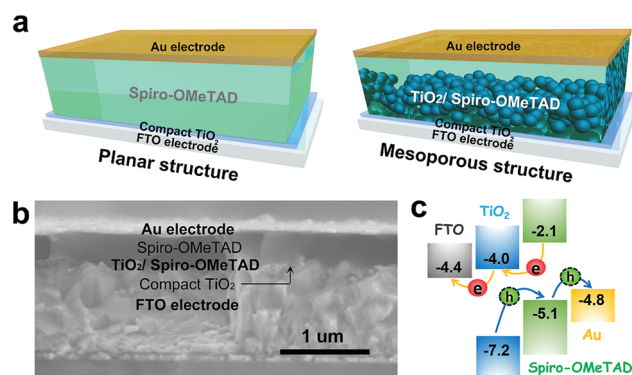

Fig. 1 (a) The device structure of the photodetector without (planar structure) and with (mesoporous structure) mesoporous TiO_2 layers. (b) The SEM cross-section image of the device with mesoporus layers. (c) The energy diagram of the photodetector.
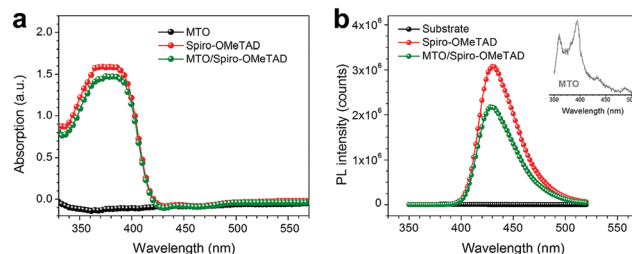

Fig. 2 (a) The absorption spectra and (b) the photoluminance spectra of MTO, spiro-OMeTAD and MTO/spiro-OMeTAD, and the inset is a larger view of MTO.

10544 | *J. Mater. Chem. C*, 2017, 5, 10543–10548

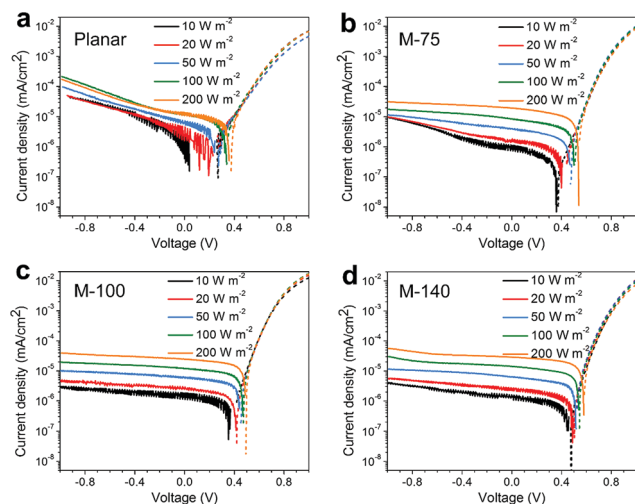This journal is © The Royal Society of Chemistry 2017

Fig. 3 Current density–voltage curves of the planar and mesoporous structured devices under ultraviolet irradiation under various power densities: (a) planar (b) M-75 (c) M-100 (d) M-140.

about 40 nm for both spiro-OMeTAD and MTO/spiro-OMeTAD. In the case of MTO/spiro-OMeTAD, the increased specific surface area produces more interfaces between mesoporous TiO$_2$ and spiro-OMeTAD films, leading to more pathways for electron injection to reduce the number of electrons from the excited state to the ground states. Thus, the photoluminescence density of the heterojunction film is lower than that of the spiro-OMeTAD film. And there are two peaks at 360 nm and 390 nm in the inset spectrum, which is a larger view of MTO, demonstrating the peaks of FTO and TiO$_2$, respectively.

The light current density–voltage characteristics of the planar and mesoporous structured photodetectors under irradiation of various ultraviolet power densities are shown in Fig. 3. It can be seen that the current densities of the all devices increase as the ultraviolet light density increases. The mesoporous devices display almost constant photocurrent density at different revise biases (−1.0 to 0 V) compared with the planar device. In addition, holes and electrons could be extracted in the mesoporous devices by a small voltage even zero. Curves of photocurrent as a function of power density with different thicknesses of TiO$_2$ layers are shown in Fig. 4a. It is clear that the photocurrent density increases with the increasing power density. The photocurrent density of the mesoporous devices is higher than that of the
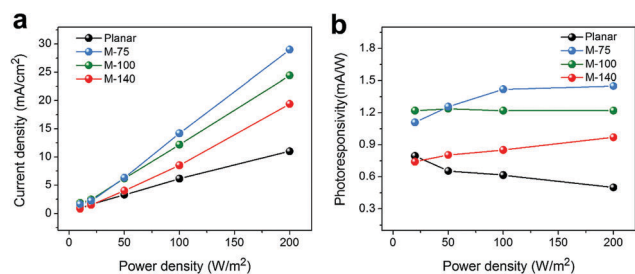
planar device. When the irradiance is 200 W m^{-2}, the photocurrent density of the M-100 device is 24.4 µA cm^{-2}, while that of the planar device is only 11.00 µA cm^{-2}. Furthermore, the photocurrent density of the mesoporous device also increases with the increasing thickness of the mesoporous TiO$_2$ layer (from 75 nm to 140 nm). Fig. 4b shows the photoresponsivity under various power densities. The photoresponsivity is defined as the ratio of photocurrent to power density.[25,26] The M-100 device displays the excellent stability among all the devices, while the value of the planar device decreases quickly with the increase of the power density. The results show that mesoporous devices have great potential in a weak ultraviolet light environment. According to the results, the performance of the mesoporous device is better than that of the planar device. The most likely reason is the large contact area between mesoporous TiO$_2$ and spiro-OMeTAD that boosts the separation of the electron–hole pairs excited by photon as well as electron injection.

The photoresponse switching performances of the devices have been measured to get accurate information about the responsiveness of the devices.[27–30] Fig. 5a and b show that both V_{oc} and the current density of the devices can be reproducibly switched from the "ON" to the "OFF" state by turning the UV light on and off periodically with a 200 W m^{-2} powder density. A fast transient voltage and current of the devices would be detected when the light is switched on. Compared to the planar device, the mesoporous devices show the higher open voltage to
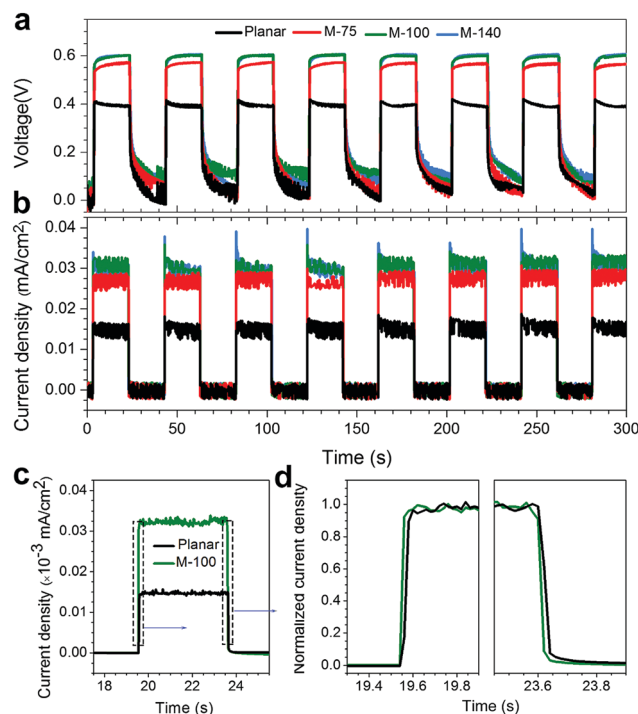

Fig. 4 (a) Current density and (b) photoresponsivity of the photodetectors under various ultraviolet power densities from 10 W m^{-2} to 200 W m^{-2} at 0 V bias voltage.

Fig. 5 Time responses of (a) open circuit voltage (V_{oc}) and (b) current density of the planar, M-75, M-100 and M-140 upon 200 W m^{-2} ultraviolet light density measured for light-on and -off states. (c) Time-resolved photocurrent density of the planar and M-100 devices. (d) Selected ranges containing particular characteristics.

the light. The voltage increases with the increasing of the mesoporous TiO_2 thickness (from 75 nm to 140 nm). The photocurrent density *versus* time response curves in Fig. 5b show the same trend, suggesting that the M-100 device displays the best performance among all devices. Besides, the M-100 device also has the highest output voltage of 0.60 V and a current density of 32.79 $\mu A\ cm^{-2}$. The reason is that thick mesoporous TiO_2 layer could accelerate the separation of holes and electrons at the interfaces of TiO_2 and spiro-OMeTAD to reduce the recombination of holes and electrons, leading to a high response to the light. Time-resolved photocurrent density of the planar and M-100 devices is shown in Fig. 5c and d. It can be seen that both the rise time and decay time of the M-100 device are much shorter than 0.02 s. While the rise time and decay time of the planar device are 0.04 s and 0.02 s, respectively, which are much longer than those of the M-100 devices. The rise time (T_r) is defined as the time for the current that increases from 10% to 90% of the peak output value. The decay time (T_f) is defined as the time for the current that decreases from 90% to 10% of the peak output value.[31–33]

Another important merit for a photodetector is responsivity (R). Responsivity is the ratio of photocurrent to incident light density, which indicates the response efficiency of the detector to the optical signal. R can be expressed by the equations:

$$R = \frac{J_{ph}}{L_{light}} \qquad (1)$$

$$R = \frac{EQE}{h\nu} \qquad (2)$$

$$D^* = R\frac{1}{\sqrt{(2qJ_d)}} \qquad (3)$$

where J_{ph} is the photocurrent, L_{light} is the incident light density and $h\nu$ is the energy of the incident photon in electronvolts.[34,35] Responsivity is proportional to the external quantum efficiency (EQE) of the photodetector as shown in eqn (2).[36,37] Therefore, it is absolutely meaningful to seek a way to improve the EQE of the photodetector. The responsivity spectra of the different structured devices are shown in Fig. 6a. The highest sensitivity

appeared at a wavelength of ∼340 nm and the photoresponse display an increase above the threshold excitation energy, 425 nm (2.9 eV), approaching the bandgap energy of spiro-OMeTAD. Obviously, the planar detector exhibits the smallest responsivity compared to that of the mesoporous device. The main reason is that the mesoporous layer introduces more injection pathways for electrons (see Fig. 2b), enhancing the photocurrent. The sensitivity of the M-100 detector is 18.29 mA W^{-1} at 340 nm wavelength with the corresponding EQE of 6.67%. The dark current–voltage characteristics of the photodetector in the dark with planar and M-100 devices are shown in Fig. 6b. With the addition of mesoporous TiO_2, the dark current density decreases faster than the planar device under revise bias. The dark current density of the planar device is 6.66 $\mu A\ cm^{-2}$, compared with this value, the dark current density of the M-100 device is 8.79 nA cm^{-2} at 0 V. It reveals that the dark current density of the M-100 device is 3 orders of magnitude lower than that of the planar device. The lower dark current density demonstrates that the M-100 device can prevent the leakage of the current, which responds to the low recombination rate of holes and electrons. While the specific detectivity (D^*) reflects the detection capability of a photoelectric detector. D^* can be calculated as presented in eqn (3), where q is the elementary charge and J_d is the dark current.[38–41] The D^* spectra of planar and M-100 devices were calculated at 0 V bias voltage as shown in Fig. 6c. D^* of the mesoporous device is much higher than that of the planar one. It can be observed that D^* of the M-100 device is more than 10^{12} Jones (1 Jones = 1 cm $Hz^{1/2}\ W^{-1}$) over the ultraviolet light region at 0 V and the highest D^* calculated to be as high as 3.5×10^{13} Jones at 340 nm, while D^* of the planar device is 3.1×10^{11} Jones. The higher D^* of the mesoporous device is mainly due to its lower dark current in comparison with the planar device under reverse bias. The mesoporous layer provides pathways for electrons that can significantly reduce the leakage current.

Fig. 7a shows the responsivity of the unencapsulated devices in the ambient air under different humidity for two months. It is clear that the responsivity of the unencapsulated devices was maintained at an almost invariable level for two months, demonstrating that the devices have excellent long term stability.
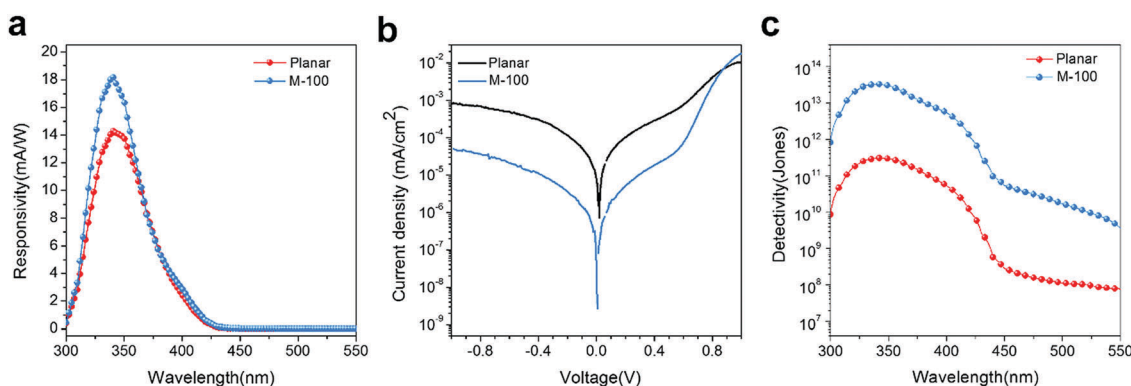

Fig. 6 (a) A spectroscopic photoresponse of the planar and M-100 devices within 300−550 nm. (b) Dark photocurrent density−voltage curves of all the devices. (c) Specific detectivity spectra calculated at 0 V bias voltage.
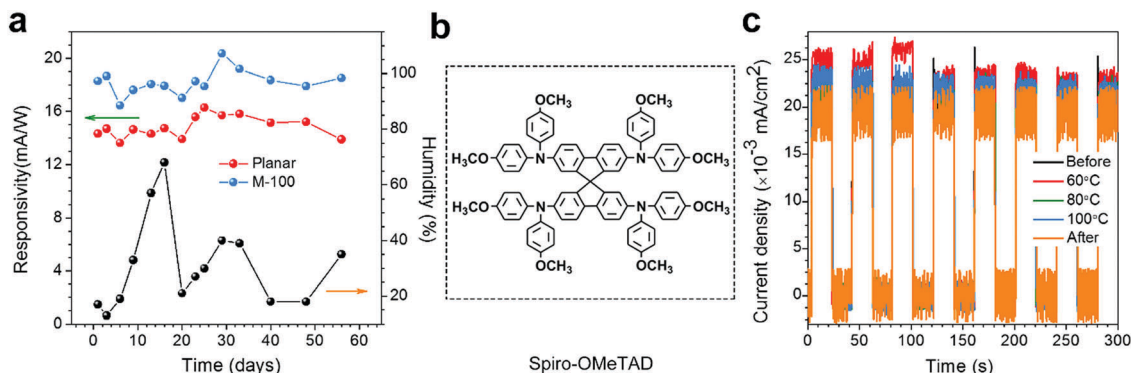
Fig. 7 (a) The responsivity of the planar and the M-100 devices in ambient air for two months under different relative humidity. (b) The chemical formula of spiro-OMeTAD. (c) Current density–time curves of the device with the mesoporous layer at different temperatures, before (at room temperature), 60 °C, 80 °C, 100 °C and after (cooling to room temperature).

Besides, from the sixth day to the twentieth day, the relative humidity increased from 19% to 68% and then decreased to 21%. There is little change in the responsivity, proving that humidity does not have a significant effect on the responsivity. As shown in Fig. 7b, there is no functional group in spiro-OMeTAD that can react with oxygen or water molecules in ambient air. Therefore, the device not only has long term stability but also has humidity resistance. Fig. 7c shows the current density–time curves of one unencapsulated mesoporous device (M-100) which was selected randomly at different temperatures, before (at room temperature), 60 °C, 80 °C, 100 °C and after (naturally cooled down to room temperature), respectively. It can be observed that the photocurrent density remains at the nearly same level when the temperature was increased from room temperature to 60 °C, 80 °C, and 100 °C. When the heated device was cooled down to room temperature, the photocurrent only has a slight change. As compared with the sample before heating, the sample after heating has the nearly identical rising and decaying times. Therefore, the device also shows the excellent thermal stability. As shown in Fig. 7b, the molecule architecture of the spiro-OMeTAD contains the benzene and ring-shaped structure, causing a great deal of energy that is required to increase the disorder, which would result in a high T_g. Consequently, spiro-OMeTAD is difficult to amorphize. Based on the above, this device has great potential for application in optical detection.

4 Conclusions

A small molecule organic semiconductor, spiro-OMeTAD, was introduced as the absorption and the hole transporting material to fabricate an ultraviolet photodetector. With a mesoporous TiO_2 layer, the charge separation efficiency of the whole device was dramatically increased. The interface recombination of FTO and spiro-OMeTAD was restricted by a well formed compact TiO_2 layer. The photodetector assembled by a 100 nm mesoporous TiO_2 film displayed a fast response time (<0.02 s), a low dark current density (8.79 nA cm^{-2}) and a high detectivity (3.5×10^{13} Jones) at a 340 nm light wavelength and a 0.60 V

voltage output. The unencapsulated device also showed the excellent long term stability and humidity resistance in ambient air for two months. Due to the molecular architecture of spiro-OMeTAD that contains the benzene and ring-shaped structure, the device has a high T_g that makes it possess good thermal stability.

Conflicts of interest

There are no conflicts to declare.

References

1 J. Herrbach, A. Revaux, D. Vuillaume and A. Kahn, *Appl. Phys. Lett.*, 2016, **109**, 073301.
2 B. Zhang, M. T. Trinh, B. Fowler, M. Ball, Q. Xu, F. Ng, M. L. Steigerwald, X. Y. Zhu, C. Nuckolls and Y. Zhong, *J. Am. Chem. Soc.*, 2016, **138**, 16426–16431.
3 P. Peumans, V. Bulović and S. R. Forrest, *Appl. Phys. Lett.*, 2000, **76**, 3855–3857.
4 H. Y. Chen, M. K. Lo, G. Yang, H. G. Monbouquette and Y. Yang, *Nat. Nanotechnol.*, 2008, **3**, 543–547.
5 J. Clark and G. Lanzani, *Nat. Photonics*, 2010, **4**, 438–446.
6 F. Yan, J. Li and S. M. Mok, *J. Appl. Phys.*, 2009, **106**, 074501.
7 Y. Qian, X. Zhang, D. Qi, L. Xie, B. K. Chandran, X. Chen and W. Huang, *Sci. China Mater.*, 2016, **59**, 589–608.
8 Y. C. Shao, Y. J. Fang, T. Li, Q. Wang, Q. F. Dong, Y. H. Deng, Y. B. Yuan, H. T. Wei, M. Y. Wang, A. Gruverman, J. Shielda and J. S. Huang, *Energy Environ. Sci.*, 2016, **9**, 1752–1759.
9 K. J. Baeg, M. Binda, D. Natali, M. Caironi and Y. Y. Noh, *Adv. Mater.*, 2013, **25**, 4267–4295.
10 Q. Wang, Y. Luo and H. Aziz, *J. Appl. Phys.*, 2010, **107**, 084506.

11 X. Li, C. Gao, H. Duan, B. Lu, X. Pan and E. Xie, *Nano Energy*, 2012, **1**, 640–645.

12 Y. Liu, J. Sun, Z. Yang, D. Yang, X. Ren, H. Xu, Z. Yang and S. F. Liu, *Adv. Opt. Mater.*, 2016, **4**, 1829–1837.

13 L. Guo, H. Zhang, D. Zhao, B. Li, Z. Zhang, M. Jiang and D. Shen, *Sens. Actuators, B*, 2012, **166–167**, 12–16.

14 Q. Tai, P. You, H. Sang, Z. Liu, C. Hu, H. L. Chan and F. Yan, *Nat. Commun.*, 2016, **7**, 11105.

15 T. Baikie, Y. N. Fang, J. M. Kadro, M. Schreyer, F. X. Wei, S. G. Mhaisalkar, M. Graetzel and T. J. White, *J. Mater. Chem. A*, 2013, **1**, 5628–5641.

16 D. Poplavskyy and J. Nelson, *J. Appl. Phys.*, 2003, **93**, 341–346.

17 A. T. Murray, J. M. Frost, C. H. Hendon, C. D. Molloy, D. R. Carbery and A. Walsh, *Chem. Commun.*, 2015, **51**, 8935–8938.

18 S. Wang, W. Yuan and Y. S. Meng, *ACS Appl. Mater. Interfaces*, 2015, **7**, 24791–24798.

19 S. Fantacci, F. De Angelis, M. K. Nazeeruddin and M. Grätzel, *J. Phys. Chem. C*, 2011, **115**, 23126–23133.

20 Y. Xie, L. Wei, Q. Li, G. Wei, D. Wang, Y. Chen, J. Jiao, S. Yan, G. Liu and L. Mei, *Appl. Phys. Lett.*, 2013, **103**, 261109.

21 O. Game, U. Singh, T. Kumari, A. Banpurkar and S. Ogale, *Nanoscale*, 2014, **6**, 503–513.

22 H. Chen, K. Liu, L. Hu, A. A. Al-Ghamdi and X. Fang, *Mater. Today*, 2015, **18**, 493–502.

23 G. Memisoglu and C. Varlikli, *Int. J. Photoenergy*, 2012, **2012**, 1–11.

24 R. Zhang, C. Fei, B. Li, H. Fu, J. Tian and G. Cao, *ACS Appl. Mater. Interfaces*, 2017, **9**, 9785–9794.

25 M. S. Pawar, P. K. Bankar, M. A. More and D. J. Late, *RSC Adv.*, 2015, **5**, 88796–88804.

26 L. Dou, Y. M. Yang, J. You, Z. Hong, W. H. Chang, G. Li and Y. Yang, *Nat. Commun.*, 2014, **5**, 5404.

27 S. Chen, C. Teng, M. Zhang, Y. Li, D. Xie and G. Shi, *Adv. Mater.*, 2016, **28**, 5969–5974.

28 C. Fei, B. Li, R. Zhang, H. Fu, J. Tian and G. Cao, *Adv. Energy Mater.*, 2017, **7**, 1602017.

29 W. Wang, F. Zhang, M. Du, L. Li, M. Zhang, K. Wang, Y. Wang, B. Hu, Y. Fang and J. Huang, *Nano Lett.*, 2017, **17**, 1995–2002.

30 S. Chen, Z. Lou, D. Chen, Z. Chen, K. Jiang and G. Shen, *Sci. China Mater.*, 2016, **59**, 173–181.

31 Z. Sun, Z. Liu, J. Li, G. A. Tai, S. P. Lau and F. Yan, *Adv. Mater.*, 2012, **24**, 5878–5883.

32 Y. Li, F. Della Valle, M. Simonnet, I. Yamada and J. J. Delaunay, *Nanotechnology*, 2009, **20**, 045501.

33 L. Gao, K. Zeng, J. Guo, C. Ge, J. Du, Y. Zhao, C. Chen, H. Deng, Y. He, H. Song, G. Niu and J. Tang, *Nano Lett.*, 2016, **16**, 7446–7454.

34 S. Han, S. M. Liu, Y. M. Lu, P. J. Cao, W. J. Liu, Y. X. Zeng, F. Jia, X. K. Liu and D. L. Zhu, *J. Alloys Compd.*, 2017, **694**, 168–174.

35 J. S. Liu, C. X. Shan, B. H. Li, Z. Z. Zhang, C. L. Yang, D. Z. Shen and X. W. Fan, *Appl. Phys. Lett.*, 2010, **97**, 251102.

36 X. Fang, Y. Bando, M. Liao, T. Zhai, U. K. Gautam, L. Li, Y. Koide and D. Golberg, *Adv. Funct. Mater.*, 2010, **20**, 500–508.

37 X. Fang, Y. Bando, M. Liao, U. K. Gautam, C. Zhi, B. Dierre, B. Liu, T. Zhai, T. Sekiguchi, Y. Koide and D. Golberg, *Adv. Mater.*, 2009, **21**, 2034–2039.

38 J. Yu, X. Chen, Y. Wang, H. Zhou, M. Xue, Y. Xu, Z. Li, C. Ye, J. Zhang, P. A. van Aken, P. D. Lund and H. Wang, *J. Mater. Chem. C*, 2016, **4**, 7302–7308.

39 G. Konstantatos, I. Howard, A. Fischer, S. Hoogland, J. Clifford, E. Klem, L. Levina and E. H. Sargent, *Nature*, 2006, **442**, 180–183.

40 S. Heo, J. Lee, S. H. Kim, D. J. Yun, J. B. Park, K. Kim, N. Kim, Y. Kim, D. Lee, K. S. Kim and H. J. Kang, *Sci. Rep.*, 2017, **7**, 1516.

41 F. Guo, B. Yang, Y. Yuan, Z. Xiao, Q. Dong, Y. Bi and J. Huang, *Nat. Nanotechnol.*, 2012, **7**, 798–802.

10548 | *J. Mater. Chem. C*, 2017, **5**, 10543–10548

This journal is © The Royal Society of Chemistry 2017